J Mater Sci (2007) 42:4650–4658
DOI 10.1007/s10853-006-0515-8

Structure of yttria stabilized zirconia beads produced by gel supported precipitation

M. Walter · J. Somers · A. Fernandez · E. D. Specht · J. D. Hunn · P. Boulet · M. A. Denecke · C. Göbel

Received: 24 May 2006 / Accepted: 5 June 2006 / Published online: 16 February 2007

Abstract Yttria stabilized zirconia (YSZ) is one of the inert matrix candidates selected for investigation as host matrix for minor actinide (MA) transmutation. The structural properties of $(Zr_{0.84}, Y_{0.16})O_{1.92}$ beads prepared by a sol–gel method for MA infiltration, are characterized as calcined (850 °C) and sintered (1,600 °C) beads. The calcined YSZ beads are fine-grained and homogenous over the entire sphere and are surrounded by a uniform outer layer of approximately 30 μm thickness. After sintering at 1,600 °C, the beads are compacted to 51% of their initial volume and exhibit a granular structure. The thermal expansion is nearly linear for the calcined material, but shows a parabolic behavior for the sintered (1,400 °C) beads. In addition, the thermal expansion of calcined material is 20–25% less than after sintering. During heating up to 1,400 °C, two processes can be distinguished. The first occurs between 900 and 1,000 °C and is related to an increase in unit cell order. The second process involves grain-growth of the less crystalline calcined material between 1,100 and 1,300 °C. These results have implications for preparation of YSZ and its use as an inert MA transmutation matix.

M. Walter (✉) · J. Somers · A. Fernandez · P. Boulet
Institute for Transuranium Elements, European Commission, Joint Research Centre, P.O. Box 2340, D-76125 Karlsruhe, Germany
e-mail: marcus.walter@ec.europa.eu

E. D. Specht · J. D. Hunn
Oak Ridge National Laboratory, P.O. Box 2008, Oak Ridge, MS 6118, USA

M. A. Denecke
Institut für Nukleare Entsorgung (INE), Forschungszentrum Karlsruhe, P.O. Box 3640, D-76021 Karlsruhe, Germany

C. Göbel
Max-Planck-Institut für Chemische Physik fester Stoffe, Nöthnitzer Str. 40, D-01187 Dresden, Germany

Introduction

Yttria stabilized zirconia (YSZ) is a high temperature ceramic material used in a variety of applications. Recently there has been considerable interest in the transmutation of actinides in nuclear reactors as a means to decrease the long-lived radiotoxic content of spent nuclear fuel. For these purposes, YSZ has also been considered as a support material for the transmutation of transuranium actinides in nuclear reactors [1–3]. YSZ is an example of a so called inert matrix fuel, as neither Zr nor Y have significant neutron capture cross sections. In contrast, the traditional fuel support matrix ($^{238}UO_2$) captures neutrons, which leads to the production of higher actinides. Thus were it used for dedicated transmutation purposes, the overall transmutation or incineration efficiency would be diminished. For this reason, the development of non-fertile matrix materials for transmutations as a novel waste disposal process are of primary importance.

Fabrication of fuels and targets for the transmutation of minor actinides (Np, Am, Cm) requires extensive innovation, as traditional powder metallurgy methods used for the production of uranium dioxide or mixed uranium–plutonium oxides (MOX)

have several drawbacks. In particular, dust poses a radiation hazard as it collects on the walls of the processing cells and on the equipment therein. Thus, novel processing routes are required to eliminate dust, and be readily adaptable to remote (telemanipulators) or automatic operation. One such technique, based on the infiltration of porous precursor beads by actinide nitrate solution has been developed and is now practiced on a laboratory scale for the production of highly radioactive fuels and targets [3]. Porous YSZ beads are produced in conventional laboratories by a sol–gel external gelation method. They are then introduced into the active cells, where they are infiltrated by the actinide nitrate solution. Following calcination, they are then compacted and sintered to give the product pellets. Alternatively, if particle fuels are required, the particles are sintered directly following calcination.

Pure ZrO_2 exists in three polymorphs at low pressure (monoclinic, tetragonal and cubic) and in an orthorhombic form at higher pressure. While the monoclinic structure is stable at room temperature, the tetragonal and cubic forms crystallize at higher temperatures. By doping with larger ions such as Y^{3+}, Er^{3+}, or Ce^{4+}, the cubic structure of ZrO_2 $(Fm\bar{3}m)$ can be stabilized at room temperature [4, 5]. Two further tetragonal ($P4_2/nmc$) YSZ polymorphs (t', t'') are known to form by transformation of cubic zirconia during quenching from high temperatures [6–8]. Both tetragonal phases differ from the ideal cubic fluorite structure by an oxygen displacement along the c-axis, which decreases with the concentration of the yttrium dopant [6, 8]. As indicated by neutron diffraction [8] and Raman spectroscopy [7] the t'/ t'' and t''/cubic phase boundaries are at $Zr_{0.86}Y_{0.14}O_{1.93}$ and $Zr_{0.82}Y_{0.18}O_{1.91}$, respectively.

In contrast to diffraction studies, which yield average long-range order information over several unit cells, Extended X-ray Absorption Fine Structure (EXAFS) spectroscopy provides information of the local, short-range order or structure, in our case of Zr and Y atoms in zirconia. In general, the local environment of the Zr atoms reflects the crystal structure (e.g., cubic, or tetragonal), whereas the environment around the dopant metal cation depends on the dopant itself [9]. The change in local structure of amorphous zirconia during heat treatment has been investigated in several EXAFS studies. Unfortunately, some of these studied only the Zr environment [10–12] or were focused on zirconias with low Y concentrations [13, 14]. An EXAFS study reported on the thermal transformation of nanocrystalline $Zr_{0.84}Y_{0.16}O_{1.92}$ films on sapphire [15] is interesting, but these results are less applicable to zirconia prepared by sol–gel process for inert matrix fuels.

This paper deals with the characterization of intermediate porous beads and their structure when sintered. A combination of scanning electron microscopy (SEM), tomography, X-ray diffraction (XRD), and EXAFS spectroscopy is used to characterize the bead structure before and after sintering over a large dimensional range: from the local structure around the atoms to the macroscopic structure of the entire particles.

Experimental

Porous bead production

Zirconyl chloride and yttrium nitrate (both Alfa Aesar) were dissolved in water and mixed in the desired proportion. An yttrium concentration of 16 mol% was selected as it is generally sufficient to give a final product with a cubic crystal structure. Polymers (methocel, Dow Chemicals) was then added to this solution to increase its viscosity [3]. The solution was then atomized and the droplets collected in an ammonia bath, where ammonia diffuses into the original droplet and causes precipitation of the hydroxides; this is the basis of the external gelation step. Due to the presence of the polymer, precipitation is geometrically controlled and confined locally, so that a droplet to particle conversion is achieved. These particles were then washed in water (or dilute ammonia) and following drying, they were calcined at 850 °C in air. During this step, the hydroxide precipitate is converted to oxide, and the polymers used in the process were removed by pyrolysis. The calcined particles are highly porous and it is this property which makes them ideally suited for actinide infiltration. Sintering of the calcined beads was also performed in air at 1,600 °C for 2 h. The heating and cooling rate was 200 K/h for both calcination and sintering.

Scanning electron microscopy (SEM)

Single calcined and sintered beads were ground in an agate mortar, in order to obtain fragments for inspection of their inner structure. In addition, some calcined and sintered beads were embedded in an epoxy resin (Spezifix20 and TEKMEK, Struers) and polished with an Al_2O_3 suspension (Logitech PM5,

grain size 9 μm). All sample surfaces were sputtered with gold for SEM investigations. SEM images of complete beads, fragments, or polished, embedded beads were recorded using a ESEM FEI Quanta 200F scanning microscope, operating at 20 kV with a field emission cathode. The microscope was arranged with a SSD-type backscattering electron (BSE) and EDT-type SE detector.

Tomography

X-ray microtomography was measured using an Xradia Micro-XCT system. A microfocus X-ray tube with a W target operating at 100 kV and 100 mA provided a 7 μm source. This source was demagnified in a projection geometry by placing the sample 40 mm from the source and 20 mm from the detector. The detector consists of a polished CsI crystal, 20 μm thick. An optical microscope images scintillation from this crystal onto a 2,048 × 2,048 pixel, 16-bit Peltier-cooled CCD camera. Resolution is estimated to be 1.7 μm. A total of 721 radiographs, each with a 10 s exposure time were measured as the sample was rotated in 0.25° increments. Tomographs were computed by parallel-beam filtered back-projection [16]. One calcined and one sintered YSZ bead were measured in this way.

X-ray diffraction

X-ray diffraction patterns of the YSZ were recorded using a Bruker D8 diffractometer ($CuK_{\alpha 1}$, Ge monochromator) equipped with an Anton Paar HTK2000 high temperature chamber, Pt-10% Rh thermocouple and a position sensitive detector (PSD-50, M. Brown). The calcined samples were heated at 1 K/s from room temperature up to 1,400 °C and diffraction patterns were recorded every 100 K. In addition, patterns were measured during subsequent cooling every 200 K down to 27 °C. The 2θ scanning range for all samples was from 25 to 120° with a 0.007° step size. Lattice parameters were obtained by Rietfeld refinement of the experimental diffraction pattern using a Pseudo-Voigt profile function within the Fullprof suite [17]. Since X-ray diffraction is less sensitive for the oxygen position of the t'' form [8], all refinement was done for the cubic $Fm\bar{3}m$ structure. An estimation of the mean crystallite size (S) of calcined YSZ beads was determined using the Scherrer-equation, $S = 0.89 \cdot \lambda / \beta \cdot \cos\,\theta$, where β is the corrected full width at half-maximum of a diffraction peak at a diffraction angle of 2θ [18].

Extended X-ray absorption fine structure (EXAFS) spectroscopy

The calcined and sintered samples were milled, mixed with boron nitride to obtain an edge jump of about one for Zr, and pressed into disks for X-ray absorption measurement. The EXAFS data at the Y and Zr K-edge were recorded at room temperature in transmission mode at the INE-beamline at the ANKA synchrotron source in Karlsruhe [19]. A pair of Ge(422) crystals are used in the double-crystal monochromator. The two Rh coated mirrors at this beamline ensure rejection of higher harmonics. The photon energy of the light coming off the DCM is calibrated against the first derivative XANES spectrum of a Zr foil, defined as 17,998 eV.

The EXAFS oscillations were extracted according to standard procedures (background removal using a polynomial preedge fit, using a cubic spline fit for removal of the atomic background, etc.) with WINXAS 3.11 [20]. The ionization threshold energy, E_0, used to define the origin for calculation of the $\chi(k)$ -function was set at the energy value of the second inflection point of the first derivative, approximately 17046 eV for Y K-edge spectra and 18014 eV for Zr specta. Theoretical phase shifts, $\delta(k)$, and backscattering amplitudes, $F(k)$, were calculated with the FEFF8 code [21] using a spherical cubic $(Zr_{0.84}Y_{0.16})O_{1.92}$ cluster with 6 Å radius, having the Cartesian coordiantes calculated from the XRD structure [7]. Because of the similar backscattering properties, the same phase shifts and amplitudes were used for Zr and Y. The amplitude reduction factor, ΔS_0^2, was held constant at 1.0 for the FEFF8 calculation and held constant at this same value for EXAFS fits. EXAFS refinements were performed with WINXAS 3.11 [20] in R-space (Zr: 0.9–3.6 Å, Y: 1.2–3.7 Å) of the Fourier transformed k^3-weighted $\chi(k)$ data (k-range Zr: 2.5–14.6 $Å^{-1}$, Y: 2.2–14.2 $Å^{-1}$).

Results

SEM observations

Both surface and inner macroscopic structure of the calcined and sintered YSZ beads was characterized by SEM measurements of complete, intact beads, bead fragments and cross-sections of beads embedded in epoxy and polished. Some representative SEM images are shown in Fig. 1. The size of the calcined (850 °C) beads, estimated from their SEM images is in the 750–860 μm range. Calcined spheres are characterized by a

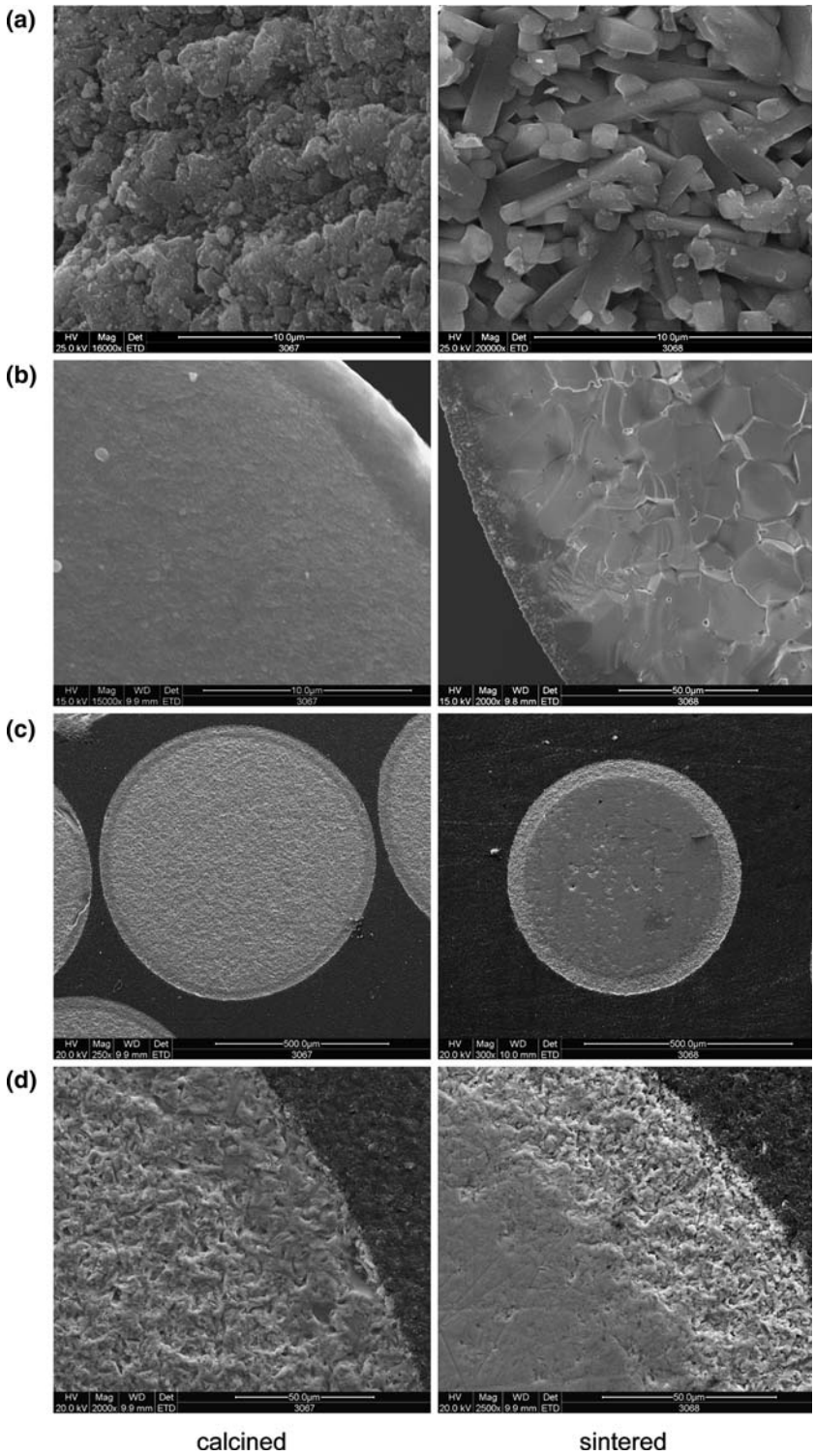

Fig. 1 SEM images of (**a**) the surface; (**b**) fracture surfaces, and (**c, d**) polished cross-sections of YSZ beads prepared by sol–gel external gelation method. Results for the calcined and sintered samples are displayed in the left and right panels, respectively

fine-grained surface which consists of small particles without any special shape. The fractured surface of calcined bead fragments show a homogeneous, microcrystalline inner structure. No larger pores or cavities are visible. In SEM images of the polished cross-sections one clearly sees that the inner part of the beads is surrounded by a surface layer. The thickness (~30 μm) of the surface layer is observed to be similar and uniform for all beads studied. In BSE images, the surface layer appears dark and the inner part more bright. Generally, a similar roughness of 2–3 μm is observed over the entire bead cross section, indicating material

homogeneity. In the surface layer zone, however, the relief left from the polishing procedure is less rough than for the inner part, which suggests that this surface layer is somewhat harder.

The size of sintered YSZ beads are estimated to be 520–600 μm in diameter from SEM images. SEM images of the sintered beads surface reveal crystals with oblong (columnar/plate) shape, up to 2 × 12 μm in size and nearly cubic shaped, approximately 1–2 μm crystals. Fragments of sintered beads show that their inner part has a crystallized structure with a grain size of approximately 20 μm. Pores of 2–5 μm are visible on grain faces, edges, and corners. A similar separation of the sintered beads into an inner part and an outer layer is found for the sintered beads as for the calcined spheres. The thickness of the outer layer seems to vary for the sintered beads, with a maximum value of about 50 μm. Polished cross-sections of the sintered beads indicate that the outer layer is rougher than the inner region.

Tomography

No evidence of any porosity appears in the tomographic sections for both calcined and sintered beads (Fig. 2). These sections appear as uniform disks: the only visible features are ring artifacts due to flaws in the detector crystal and a bright ring near the surface of the sphere to due hardening of the polychromatic X-ray beam [16]. This implies that the pore size is below the 1.7 μm instrumental resolution.

As expected, sintering increases the density of the YSZ beads. The tomographic sections measure the absorption of the polychromatic X-ray beam, which changes with the hardening of the X-ray spectrum and is not readily translated into density units, but serves well as a measure of relative density. Such an analysis indicates that the density increases by 46% upon sintering as the absorption ranges from 15.6 to 38.9 cm^{-1} before sintering and from 22.6 to 57.7 cm^{-1} after sintering. The bead diameter decreases from 800 to 640 μm. Beam hardening artifacts obscure any density variations which may occur near the particle surface.

X-ray diffraction

Typical X-ray diffraction patterns of the YSZ beads calcined at 850 °C and of the same sample after heating up to 1,400 °C (sintered) are shown in Fig. 3a and b, respectively. The mean crystallite size of calcined YSZ beads is estimated to be 16 nm from the diffraction pattern. Heating to 1,400 °C brings crystal growth, as can be seen from the (400) reflection peak shapes depicted in the inset of Fig. 3. Except for the shift due to thermal expansion, there is no change in peak shape up to 1,000 °C. Between 1,000 and 1,300 °C the diffraction peaks become sharper, but have similar width at 1,300 and 1,400 °C, indicating that the crystal growth occurs mainly between 1,100 and 1,300 °C. It should be noted that there is no indication of any splitting of the (400) peak, which would indicate the presence of tetragonal YSZ in the t or t' form.

The thermal dependence of the refined lattice parameter is shown in Fig. 4 and Table 1. Comparison of results during heating and cooling after sintering shows that the lattice parameter of the sol–gel prepared YSZ beads is greater after the sintering procedure. The lattice constant of the calcined beads increases nearly linearly with temperature up to 800 °C and the linear expansion coefficient (α_{lin}) is $8.5(2) \times 10^{-6}\ K^{-1}$ in this range. The data points at 900 and 1,000 °C exhibit an anomalous stepwise increase in lattice parameter. Above 1,200 °C identical lattice parameter values are observed both during heating up and cooling down of the sample. During the cooling down cycle, i.e., after sintering has been completed, the

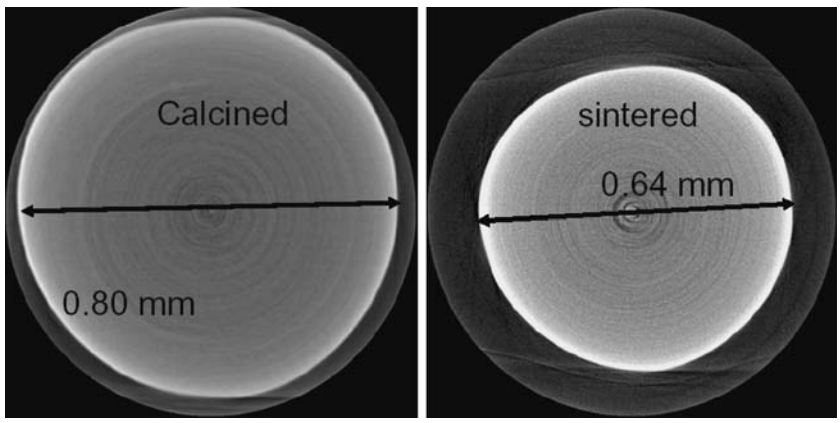

Fig. 2 Tomographic cross sections of calcined and sintered YSZ beads

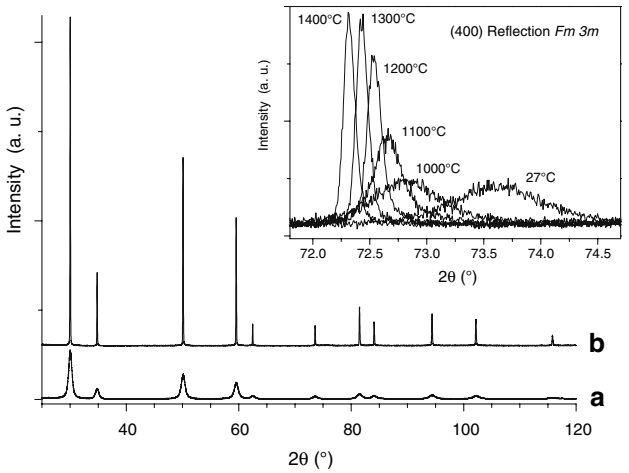

Fig. 3 X-ray pattern of calcined YSZ beads prior to (**a**) and after heating up to 1,400 °C; (**b**). Both diffraction patterns were recorded at room temperature. The inset shows the behavior of the (400) reflection ($Fm\bar{3}m$) with increasing temperature. Crystallization starts at 1,000 °C and is finished by 1,300 °C

lattice parameter values exibit a deviation from a linear thermal expansion behavior. If the linear behavior is assumed, the thermal expansion factor α_{lin} is $1.14(3) \times 10^{-5}$ K^{-1}. We apply the parabolic approach of Terblanche [22] to fit the non-linear thermal dependence for the cooling down measurements of the beads according to the expression

$$a_0 = a_0\,(300\text{K}) + a_1 \cdot (\text{T} - 273\ \text{K}) + a_2 \cdot (\text{T} - 273\ \text{K})^2$$

where $\alpha_1 = 8.59(7) \times 10^{-6}$ K^{-1} and $\alpha_2 = 1.90(5) \times 10^{-9}$ K^{-2}. The obtained values agree well with thermal expansion coefficients determined by Terblanche [22] for YSZ with 17.2–38.7 mol% Y. This parabolic fitting was also applied

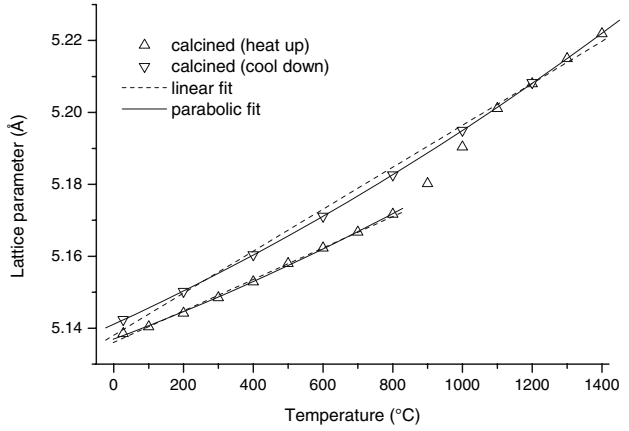

Fig. 4 Lattice parameter ($Fm\bar{3}m$) of calcined YSZ beads as function of temperature during heating (Δ) and subsequent cooling down (∇)

for the thermal expansion of the calcined beads during the initial heating up to 800 °C, yielding $\alpha_1 = 7.1(4) \times 10^{-6}$ K^{-1} and $\alpha_2 = 1.8(5) \times 10^{-9}$ K^{-2}. However, the thermal expansion of the calcined sol–gel derived YSZ beads is significantly lower by about 20–25% compared with the sintered samples.

EXAFS results

The Zr K-edge EXAFS spectra of both calcined and sintered YSZ samples are depicted in Fig. 5. Qualitative inspection of the two spectra shows them to have a similar EXAFS pattern; however, the amplitude of their EXAFS oscillations differs. This is also evident in their corresponding Fourier transforms (FT). Two significant FT peaks are observed. The second FT peak near 3.2 Å (R + Δ) in the sintered sample, resulting from backscattering on neighboring Zr(Y), exhibits significantly greater intensity than the second FT peak in the calcined sample. In contrast, the first FT peak at 1.6 Å (R + Δ), which is associated with scattering on neighboring O atoms lying nearest to Zr, remains nearly constant after sintering.

The k^3-weighted Y K-edge EXAFS spectra and their corresponding FT spectra are shown in Fig. 6. The same general trend is observed at the Y K-edge as for the Zr K-edge: significant increase in the second FT peak intensity following sintering. However, the increase is greater for the Y K-edge data. This suggests that the sintering step induces a significant ordering of the Y–Zr(Y) coordination shell compared to the Zr–Zr(Y) shell. The Zr and Y edge EXAFS results of the sintered sample are very similar to that reported in the literature [23].

The FT of the EXAFS spectra were fitted using a two shell model (Table 2). Since both the coordination number N and the Debye–Waller factor σ^2 contribute to the amplitude of an EXAFS oscillations, they are highly correlated with one another. Therefore, the coordination numbers N were held constant in the fit model at values expected in the ideal $Fm\bar{3}m$ crystal structure. In this way comparable values for σ^2 are obtained. Keeping in mind that the aliovalent Y dopant creates oxygen vacancies (one O for every two Y atoms), the N might be somewhat smaller than the ideal $Fm\bar{3}m$ crystallographic value of 8. However, we consider the expected real difference in N caused by the aliovalent cation to be within the accuracy of the EXAFS method in the experimental determination of N (±20%).

For both calcined and sintered YSZ, the observed interatomic Zr–O distance is 2.14–2.15 Å; the value for Y–O is 2.30 Å. The second nearest neighbor shell

Table 1 Lattice parameters (in Å) of calcined sol–gel prepared YSZ upon heating to temperatures between 27 and 1,400 °C and subsequent colling down to 27 °C

Temperature (°C)	Heat up	Cool down
27	5.1385[a]	5.1424[b]
100	5.1404[a]	–
200	5.1442[a]	5.1502[b]
300	5.1485[a]	–
400	5.1529[a]	5.1604[b]
500	5.1580[a]	–
600	5.1623[a]	5.1711[b]
700	5.1667[a]	–
800	5.1717[a]	5.1826[b]
900	5.1802	–
1,000	5.1904	5.1950[b]
1,100	5.2011	–
1,200	5.2080	5.2083[b]
1,300	5.2150[b]	–
1,400	5.2219[b]	–

[a] Data used for calculation of the thermal expansion of calcined YSZ

[b] Data used for calculation of the thermal expansion of sintered YSZ

Zr–Zr(Y) distances are 3.57–3.58 Å and Y–Zr(Y) distances are 3.61 Å. Due to their nearly identical backscattering properties it is not possible to distinguish Zr and Y in the second shell. There is no discernible difference in the bond lengths before and after sintering, since the typical experimental limit of the EXAFS method is 0.01–0.02 Å.

Our results are in accord with most of the EXAFS investigations reported on cubic ZrO_2–$YO_{1.5}$. Mean distance reported for the first oxygen shell are approximately 2.10–2.17 Å for Zr–O and 2.28–2.33 Å for Y–O [15, 23–26]. In the tetragonal *t* form the Zr–O shell is split [10, 12, 23, 25]. The mean Y-cation and Zr-cation distances of both *t* and cubic forms are near 3.6 Å and do not differ from one another. According to the studies of Catlow et al. [24], Veal et al. [27] and Li et al. [23] the oxygen vacancy resulting from the aliovalent yttrium dopant is associated with the Zr forming $^{[7]}$Zr polyhedra instead of $^{[8]}$Zr and partly $^{[7]}$Y polyhedra instead of $^{[8]}$Y at higher Y concentrations [27].

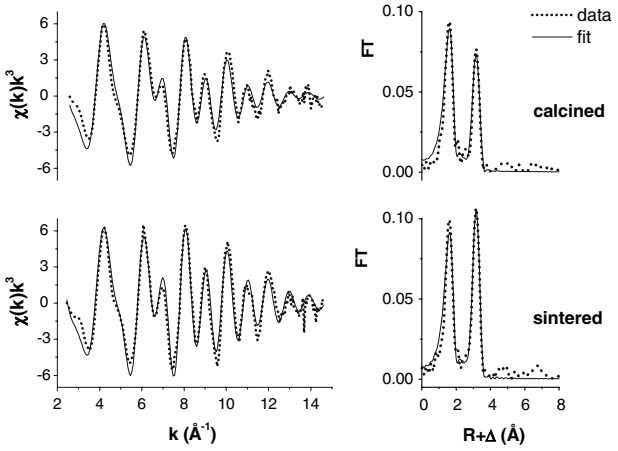

Fig. 5 Experimental k^3-weighted Zr K-edge EXAFS spectra and corresponding Fourier transforms of calcined (top) and sintered YSZ (bottom). Theoretical fit curves are also shown

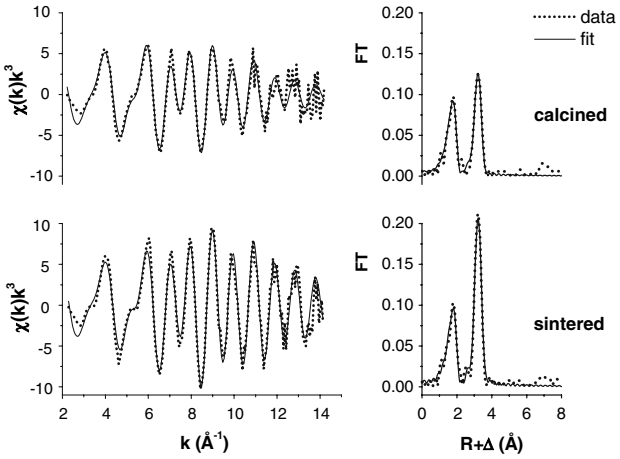

Fig. 6 Experimental k^3-weighted Y K-edge EXAFS spectra and corresponding Fourier transforms of calcined (top) and sintered YSZ (bottom). Theoretical fit curves are also shown

Inspection of σ^2 values obtained in the fits and listed in Table 2 for Zr–O and Y–O shows them to remain nearly constant (0.010 ± 0.001 Å^2) for both the calcined and sintered samples. This appears not to be the case for the second coordination shell, especially the Y–Zr(Y) shell, where σ^2 is reduced significantly for the sintered sample. This indicates that the structural disorder of the Zr(Y) shell surrounding Y atom in sintered YSZ is less than that for Zr atoms. This is in accord with our conclusion based on qualitative inspection of intensity changes in the FT spectra discussed above. The higher disordered environment around Zr can be attributed to an offset of Zr atoms from the ideal crystallographic *4a* position, due to the partial formation of $^{[7]}$Zr instead of $^{[8]}$Zr polyhedra induced by oxygen vacancies introduced into the lattice upon introduction of trivalent Y [9, 24].

Discussion

Sintering changes on the macroscopic scale

Based on the diameters determined by microscopy and tomography for calcined and for sintered YSZ beads, there is a loss of sphere volume of 46–49% during the

Table 2 Structural parameters obtained for fits to the EXAFS data shown in Figs. 5 and 6 for Zr and Y in YSZ (see text for details)

Sample	Shell	N[a]	R (Å)[b]	σ^2 (Å^2)[c]	Residuals[d]
Zr K–edge					
calcined	Zr–O	8	2.14	0.012	0.45
	Zr–Zr/Y	12	3.58	0.013	
sintered	Zr–O	8	2.15	0.011	0.51
	Zr–Zr/Y	12	3.57	0.011	
Y K–edge					
calcined	Y–O	8	2.30	0.0096	1.11
	Y–Zr/Y	12	3.61	0.0098	
sintered	Y–O	8	2.30	0.0092	1.34
	Y–Zr/Y	12	3.61	0.0070	

[a] N coordination number (held constant during the fit)

[b] R radial interatomic distance

[c] σ^2, Debye–Waller factor, estimated error $\Delta\sigma^2 = 10\%$

[d] Residuals are given as the normalized fit error $\Sigma[\chi_{data}(k)\cdot k^3 - \chi_{fit}(k)\cdot k^3]^2/(P - F)$; (P number of data points, F number of variables.)

sintering process. Even though some pores remain in the sintered beads and the lattice parameter at room temperature increases slightly, the loss in sphere volume can be attributed to the elimination of the porosity of the calcined beads. The size of the pores in the calcined beads could not be derived from SEM or tomography, and must be lower than 1 μm. Consequently, the infiltrated actinide forms particles definitely less than 1 μm in size within the YSZ beads so that a homogenous $(Zr,Y,MA)O_{2-x}$ can be observed after sintering [3].

Besides the increase in material density, thermal treatment of calcined YSZ beads leads to significant changes in the macroscopic and microscopic structure. Starting from the fine-grained texture of calcined YSZ, the sintered material shows a coarse grain structure. This is accompanied by an increase in crystal size from 16 nm (XRD) for calcined beads to about 1–20 μm (SEM) for the sintered ones. Ultimately for the final application as a transmutation target, the grain size of the sintered material plays an important role in inhibiting (or delaying) release of volatile fission products into the pores, and eventually by grain boundary diffusion to the periphery of the sample, where it is released to the plenum.

An interesting aspect is the outer layer present on both calcined and sintered beads, which for the calcined samples, is somewhat harder than the inner bulk material. The origin of this layer is certainly an artifact of the production process and could have been caused in the initial stages of the external gelation process, as the ammonia diffuses from the surrounding liquid into the droplet, and it is this outer layer that precipitation first occurs. Further ammonia has then to pass this layer and the inner region potentially may precipitate in a different way, simply because the ammonia delivery rate is different. In the calcination step, heat is also transferred from the outside to the inner regions, and this affect the surface region in a more profound way than the interior. Sintering cause the layer to develop, but its thickness is more variant, which would lend support to the thermal processing being the cause of this outer layer structure. A dense outer layer could perturb the inert matrix fuel production by the infiltration process. However, such an effect has not been observed in infiltration tests [3], but restriction of the infiltration to (larger) surface layers can occur if the infiltration is performed in such a way as that there is no release mechanism for trapped air inside the particle. If this layer is in fact mechanically less stable, it could be susceptible to abrasion, which could be an issue in certain applications (e.g., chemical vapor deposition of coatings in a fluidized bed).

Sintering changes on the nanoscale

In addition to the macroscopic processes, sintering alters the ordering of the atoms within the crystal structure. Two different processes, one at 900–1,000 °C and the other at 1,100–1,300 °C, can be distinguished from lattice parameter determinations as a function of temperature (Fig. 4) and associated thermal expansion. At lower heating temperatures of the calcined beads (900–1,000 °C), a step-like decrease in the difference between the lattice constant measured during heating and that during subsequent cooling is observed, which can be attributed to an increase in the unit cell order. This order involve O vacancy ordering and/or ordering of Y atoms in the metal cation sublattice. Sharpening of diffraction peaks is observed at temperatures between 1,100 and 1,300 °C as the crystals grow and crystallite size increases. This is in agreement with SEM measurements and with the observation that diffusion controlled grain growth, i.e., sintering, starts

at temperatures around 1,200 °C [28]. Above 1,300 °C, the crystallite size continues to increase, but the influence of grain size on the peak shape becomes small with respect to the instrumental resolution and thermal vibrations within the lattice.

EXAFS results show that the effect of sintering on the local metal disorder is different for Y and Zr. This reflects an ordering process on the unit cell scale, since crystal growth should affect the surroundings of both metals with the same magnitude. Starting from a poorly ordered YSZ, as is present in the calcined beads, the change in lattice constant between 900 and 1,000 °C is most likely attributed to ordering of O vacancies around Zr.

Conclusions

Porous calcined YSZ beads ($Zr_{0.84}Y_{0.16}O_{1.92}$) produced by sol–gel external gelation (gel supported precipitation) method consist of a homogenous fine-grained material. The beads are surrounded by a uniform outer layer, which appears somewhat harder than the inner material. During sintering, the texture of the material becomes granular. These macroscopic changes during sintering are accompanied by an increase in crystallinity and crystal growth. The associated ordering changes in local metal structure is different for Y and Zr on the unit cell scale. These results provide a basis for understanding processes involved in the infiltration method for the fabrication of MA doped inert matrix fuels such as $(Zr,Y,Am)O_{2-x}$. Future investigations will consider structural studies on the incorporation of the actinide into the crystal structure during the course of the thermal treatments.

Acknowledgements We would like to acknowledge the assistance of Y. Martin Alvarez and H. Hein in the preparation of samples, J. Rothe and K. Dardenne for assistance using the INE-beamline, and thank the *ANKA Angstroemquelle Karlsruhe* for providing beamtime for the EXAFS measurements. X-ray tomography at ORNL was sponsored by the Office of Nuclear Energy, Science and Technology and Oak Ridge National Laboratory, managed by UT-Battelle, LLC, for the U.S. Department of Energy under contract No. DE-ACO5-00OR22725.

References

1. Degueldre C, Paratte JM (1999) J Nucl Mater 274:1
2. Raison PE, Haire RG (2001) Progress Nucl Energy 38:251
3. Fernández A, Haas D, Konings RJ, Somers J (2002) J Am Ceram Soc 85:694
4. Scott HG (1975) J Mater Sci 10:1527
5. Yashima M, Kakihana M, Yoshimura M (1996) Solid State Ionics 86–88:1131
6. Zhou Y, Lei T-C, Sakuma T (1991) J Am Ceram Soc 74:633
7. Yashima M, Ohtake K, Arashi H, Kakihana M, Yoshimura M (1993) J Appl Phys 74:7603
8. Yashima M, Sasaki S, Kakihana M (1994) Acta Cryst B 50:663
9. Li P, Chen I-W, Penner-Hahn JE (1994) J Am Ceram Soc 77:118
10. Antonioli G, Lottici PP, Manzini I, Gnappi G, Montenero A, Paloschi F, Parent P (1994) J Non-Cryst Solids 177:179
11. Wang Y, Lu K, Wang D, Wu Z, Fang Z (1994) J Phys Condens Matter 6:633
12. Chadwick AV, Mountjoy G, Nield VM, Poplett IJF, Smith ME, Strange JH, Tucker MG (2001) Chem Mater 13:1219
13. Jiménez-Solís C, Esquivias L, Prieto C (1995) J Alloy Compd 228:188
14. Qi Z, Shi C, Wei Y, Wang Z, Liu T, Hu T, Zhao Z, Li F (2001) J Phys Condens Matter 13:11503
15. Rush GE, Chadwick AV, Kosacki I, Anderson HU (2000) J Phys Chem B 104:9597
16. Kak AC, Slaney M (eds) Principles of computerized tomographic imaging (Society for Industrial and Applied Mathematics, Philadelphia, 2001)
17. Rodriguez-Carvajal J FULLPROF version 3.00 (ILL, November 2004, unpublished)
18. Klug HP, Alexander LE (1974) X-ray procedures. Wiley, New York
19. Denecke MA, Rothe J, Dardenne K, Blank H, Hormes J (2005) Physika Scripta T115:1001
20. Ressler T, (1998) J Synchrotron Rad 5:118
21. Ankudinov AL, Ravel B, Rehr JJ, Conradson SD, (1998) Phys Rev B 58:7565
22. Terblanche SP, (1989) J Appl Cryst 22:283
23. Li P, Chen I-W, Penner-Hahn JE, (1993) Phys Rev B 48:10074
24. Catlow CRA, Chadwick AV, Greaves GN, Moroney LM, (1986) J Am Ceram Soc 69:272
25. Tuilier MH, Dexpert-Ghys J, Dexpert H, Lagarde P, (1987) J Solid State Chem 69:153
26. Ishizawa N, Matsushima Y, Hayashi M, Ueki M, (1999) Acta Cryst B 55:726
27. Veal BW, McKale AG, Paulikas AP, Rothman SJ, Nowicki LJ, (1988) Physica B 150:234
28. Clark JN, Glasson DR, Jayaweera SAA, (1987) Rev Chim Miner 24:654